

Available online at www.sciencedirect.com

SciVerse ScienceDirect

www.elsevier.com/locate/jmbbm

Research Paper

Effect of high-energy X-ray irradiation on creep mechanisms in bone and dentin

Alix C. Deymier-Black^{a,*}, Anjali Singhal^a, Fang Yuan^a, Jonathan D. Almer^b,
L. Catherine Brinson^c, David C. Dunand^a

^aDepartment of Materials Science and Engineering, Northwestern University, Evanston, IL 60208, USA

^bX-ray Science Division, Advanced Photon Source, Argonne National Laboratory, Argonne, IL 60439, USA

^cDepartment of Mechanical Engineering and Department of Materials Science and Engineering, Northwestern University, Evanston, IL, 60208, USA

ARTICLE INFO

Article history:

Received 6 November 2012

Received in revised form

8 January 2013

Accepted 23 January 2013

Available online 1 February 2013

Keywords:

Bone

Dentin

Creep

Synchrotron

X-ray diffraction

Irradiation damage

ABSTRACT

Under long-term loading creep conditions, mineralized biological tissues like bone are expected to behave in a similar manner to synthetic composites where the creeping matrix sheds load to the elastic reinforcement as creep deformation progresses. To study this mechanism in biological composites, creep experiments were performed at 37 °C on bovine compact bone and dentin. Static compressive stresses were applied to the samples, while wide- and small-angle scattering patterns from high energy synchrotron X-rays were used to determine, respectively, the elastic strain in the hydroxyapatite (HAP) platelets and the strain in the mineralized collagen fibril, as a function of creep time. In these highly irradiated biological composites, the reinforcing hydroxyapatite platelets progressively transfer some of their stress back to the softer protein matrix during creep. While such behavior can be explained by damage at the interface between the two phases, it is not consistent with measurements of the apparent moduli – the ratio of applied stress to elastic HAP strain measured throughout the creep experiments by elastic unload/load segments – which remained constant throughout the experiment and thus indicated good HAP/protein bonding. A possible explanation is a combination of X-ray and load induced interfacial damage explaining the shedding of load from the HAP during long term creep, coupled with interfacial re-bonding of the load-disrupted reversible bonds upon unloading, explaining the unaffected elastic load partitioning during unload/load segments. This hypothesis is further supported by finite element modeling which shows results mirroring the experimental strain measurements when considering interfacial delamination and a compliant interstitial space at the ends of the HAP platelets.

© 2013 Published by Elsevier Ltd.

*Corresponding author. Tel.: +1 520 248 1956; fax: +1 314 454 5047.

E-mail addresses: a.black@wustl.edu, francedanceall@yahoo.com, alixdeymier2010@u.northwestern.edu, alix.c.black@gmail.com (A.C. Deymier-Black), anjalisinghal2007@u.northwestern.edu (A. Singhal), FangYuan2008@u.northwestern.edu (F. Yuan), almer@aps.anl.gov (J.D. Almer), cbrinson@northwestern.edu (L.C. Brinson), dunand@northwestern.edu (D.C. Dunand).

¹Presently at: Department of Orthopedic Surgery, Washington University in St Louis School of Medicine, 660 S. Euclid Ave, St Louis, MO 63110, USA.

1. Introduction

Ionizing radiation is an important and widely used tool in the medical research fields where it is commonly employed, with a range of doses, on or near mineralized tissues such as bones and teeth. At the lowest doses, 7–60 Gy, ionizing radiation is used in the treatment of cancers (Fränzel and Gerlach, 2009; Kielbassa et al., 2006; Thariat et al., 2010). It is also widely employed as a sterilization tool where doses of 17–30 kGy are often used to treat bone allografts, greatly decreasing the transmittal of bacterial diseases after implantation (Nguyen et al., 2007a, 2007b; Dziedzic-Goclawska et al., 2005; White et al., 1994). More recently, synchrotron X-rays have been used to study the organization, structure, and mechanical properties of materials such as bone and teeth exposing them to doses ranging from tens to thousands of kilograys (Akhtar et al., 2008a, 2008b; Almer and Stock, 2005, 2007; Deymier-Black et al., 2010; Gupta et al., 2006a, 2006b, 2005). Although all of these methods have proven to be extremely useful, there is evidence that both low (Fränzel and Gerlach, 2009; Nguyen et al., 2007a; Cornu et al., 2000; Currey et al., 1997; Nyman et al., 2005) and high (Barth et al., 2010, 2011) doses of irradiation may have significant side effects on the mechanical behavior of bone and dentin.

The effect of irradiation on bone and dentin is not completely understood; however, it is theorized that irradiation most likely affects the collagen and its interaction with the mineral, a carbonated biological hydroxyapatite (HAP). Collagen, the proteinaceous phase of bone and dentin, acts as a viscoelastic material allowing hard, collagen-based biological materials such as bone and dentin to be tough and crack resistant (Zioupou et al., 1999; Wang et al., 2001; Vashisth, 2004; Ritchie et al., 2009; Ritchie, 2011; Kruzic et al., 2003; Kahler et al., 2003; El Mowafy and Watts, 1986). However, it has been observed that after irradiation collagen undergoes scission on the collagen backbone and increased crosslinking between collagen fibers (Nguyen et al., 2007a; Dziedzic-Goclawska et al., 2005). Both of these cases cause significant changes in the collagen behavior, greatly affecting the post-yield properties of composites like bone and dentin. It has also been suggested that irradiation may promote decarboxylation of protein side chains thus damaging the interface between the proteinaceous collagen matrix and the HAP platelets (Hubner et al., 2005; Kolovou and Anastassopoulou, 2007). The change in interfacial strength and collagen mechanical properties due to high irradiation doses results in a reduction of fracture toughness, ultimate strength, work to failure, bending strength, impact energy absorption, and fatigue failure (Cornu et al., 2000; Currey et al., 1997; Barth et al., 2010, 2011; Akkus et al., 2005). Most previous studies have investigated the effect of low doses of irradiation on bone mechanics; however, with increasing use of synchrotron radiation to investigate the properties of biological materials (Akhtar et al., 2008a, 2008b, 2011; Almer and Stock, 2005, 2007, 2010; Gupta et al., 2006a, 2006b, 2005; Barth et al., 2010, 2011; Al-Jawad et al., 2007; Neil Dong et al., 2010), it is becoming important to determine the effect of high irradiation doses on bone and dentin. In this study, the effect of high-dose, high-energy synchrotron X-ray

irradiation on the creep properties of bone and dentin will be investigated.

Creep, which is the tendency of an object to permanently deform over time due to stress, has been observed in both bone and dentin (Bowman et al., 1994; Jantararat et al., 2002). Although creep at high stresses is rarely a biologically relevant loading mode for bone and dentin, it is highly relevant in the case of surgical and orthodontic procedures (Bolotin et al., 2007; Ren et al., 2003). It also probes the viscoelastic and interfacial properties of bone and dentin. Previous work has investigated the strain evolution of HAP and mineralized fibrils in bone subjected to creep at relatively low radiation doses (~50 kGy), using synchrotron X-ray diffraction (Deymier-Black et al., 2012a). This study showed that, with continuing creep time, load is transferred from the collagen phase to the stiffer HAP phase, as expected (and observed experimentally) in synthetic composites with strongly bonded interfaces (Madgwick et al., 2002; Winand et al., 2000). However, in the current study, it is theorized that X-ray irradiation degrades the HAP–collagen interface, compromising the ability of collagen to transfer load to HAP during creep deformation, and thus affecting the creep properties of the material. To investigate this hypothesis, synchrotron X-ray diffraction was used to measure the strain evolution in the HAP and mineralized collagen fibrils of irradiated bone and dentin, and a finite element model was developed to explain the results obtained.

2. Materials and methods

2.1. Sample preparation

Bone and dentin samples were prepared as described in our previous studies (Deymier-Black et al., 2010, 2011, 2012a, 2012b; Singhal et al., 2011) and as summarized here. Bovine femurs of a healthy 18-month old Black Angus cow were obtained within an hour after slaughter. They were stored in phosphate-buffered saline (PBS) at a temperature of -20°C . The bones were thawed and cut with a low-speed diamond saw using low cutting rates and constant lubrication and cooling with DI water to create two cortical bone cuboids of dimensions $5.1 (\pm 0.004) \times 4.1 (\pm 0.036) \times 3.0 (\pm 0.019) \text{ mm}^3$, one from the posterior and one from the anterior end, with the largest dimension oriented along the long-axis of the femur. The mechanical properties of the two samples are not expected to be different (Singhal et al., 2012).

Incisors were extracted from the lower mandible of a different 18-month old Black Angus cow within an hour after death. The front incisors were extracted and stored in 1% antibacterial and antifungal solution in PBS, and frozen at -20°C . Parallel cuts were made below the enamel–cementum junction and perpendicular to the direction of growth of a thawed second incisor from the right side of the jaw. This resulted in two adjacent root dentin samples with heights of $7.4 (\pm 0.03) \text{ mm}$ and the natural tooth cross-section. Bone and dentin samples were frozen in PBS at -20°C until the time of the experiment.

2.2. Diffraction measurements

All the mechanical tests were performed at the 1-ID-C beamline of the Advanced Photon Source (APS) at Argonne National Laboratory as described previously (Deymier-Black et al., 2012a, 2011, 2012b; Singhal et al., 2011). Compressive load was applied with an MTS 858 load frame with a customized base and hydraulic loading. The lower compression platen was adapted to maintain the hydration state of the samples during loading. All tests were performed at 37 °C, close to bovine body temperature.

2.2.1. Static creep tests

Creep tests were performed on both bone and dentin samples as described previously (Deymier-Black et al., 2012a). For bone, X-ray measurements were made at the vertical and horizontal center of a single sample from the posterior end of the femur. The beam passed transverse to the long-axis of the bone. The sample was loaded along the bone long-axis direction. Similarly, a single root-dentin cylinder, taken from directly below the enamel–cementum junction, was positioned so that load was applied parallel to the root long-axis. The beam traversed the sample at the vertical and horizontal center of the sample in the mesial–distal direction. Both samples were loaded compressively to –95 MPa in ~5 s and maintained at this constant stress for 3 h. Wide Angle X-ray Scattering (WAXS) and Small Angle X-ray Scattering

(SAXS) diffraction patterns were recorded at intervals of 5 min.

A monochromatic X-ray beam with 65 keV energy and a $50 \times 50 \mu\text{m}^2$ cross-section was directed at the sample perpendicular to its loading direction, as shown in Fig. 1. The diffraction patterns were collected on area detectors placed behind the sample, nominally perpendicular to the direction of the beam. Irradiation conditions resulted in radiation doses of 17.7 kGy per combined WAXS/SAXS measurement and an accumulated dose of 637 kGy.

2.2.2. Interval creep tests

The interval creep tests consist of repeated load–creep–unload cycles on the bone and dentin samples. These experiments were set-up in the same way as the static creep tests described in the previous section. One exception for the dentin samples is that three measurements were made on a single sample taken 8 mm below the enamel–cementum junction: at the vertical and horizontal center of the cylinder as well as 1 mm to either side of the center. In all three cases, the beam passed through the dentin in the mesial–distal direction. The bone sample was taken from the anterior end of the femur. Both the bone and dentin samples were loaded to –95 MPa in ~5 s and the load was maintained for 1 h. During that first hour, WAXS and SAXS measurements were taken every 3 min at the same locations. The sample was then unloaded to 0 MPa in –19 MPa decrements and immediately reloaded to –95 MPa with the same increments.

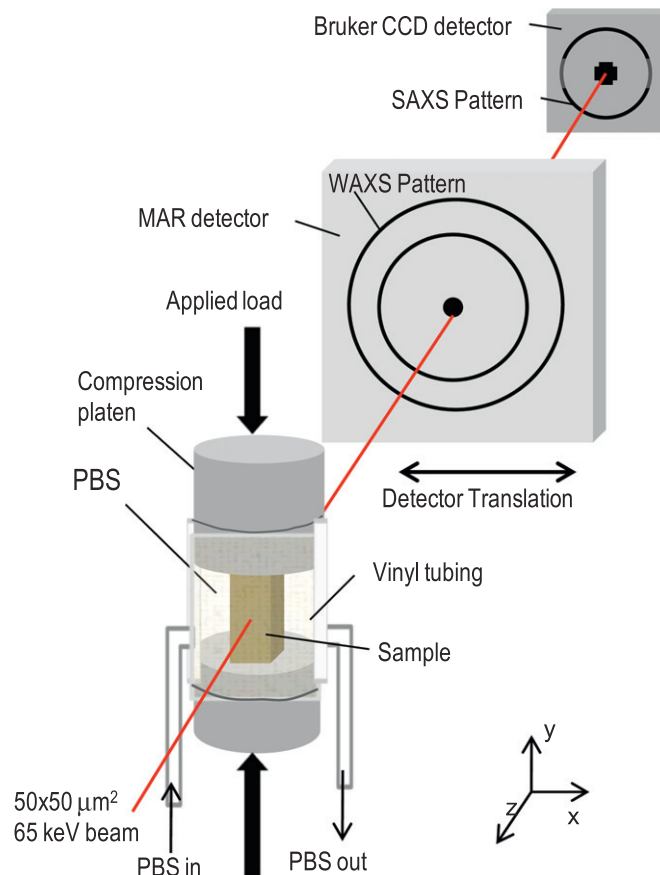


Fig. 1 – Schematic of the experimental diffraction setup.

At each increment, WAXS and SAXS patterns were obtained. Once reloaded, the cycle of creep, unloading and reloading was repeated twice.

For the bone sample, an X-ray beam with an energy of 78 keV and a cross section of $50 \times 50 \mu\text{m}^2$ was used. Irradiation conditions resulted in a radiation dose of 62 kGy per WAXS/SAXS measurement and an accumulated dose of 8034 kGy. The dentin had a reduced radiation dose of 26.6 kGy per combined WAXS/SAXS measurement with a total accumulated dose of 1730 kGy.

2.3. Diffraction analysis

2.3.1. Strain analysis

The strains as calculated from the WAXS and SAXS data are determined as described in the literature (Almer and Stock, 2007; Deymier-Black et al., 2010), and summarized here. Changes in lattice spacing in the HAP are used to determine elastic strains in the mineral phase described here as HAP strains. HAP diffraction rings are fitted using a pseudo-Voigt model which determines the peak center for each ring of interest (HAP (00.2) and HAP(00.4) in our case) at various azimuthal angles, $R(\eta)$. When plotting radial peak center, $R(\eta)$, as a function of azimuth, η , at multiple stress levels, the lines intersect at a single radius R^* called the invariant radius. R^* represents the stress-free point and is used to calculate the orientation-dependent deviatoric strains using the equation:

$$\varepsilon(\eta) = \frac{(R^* - R(\eta))}{R(\eta)} \quad (1)$$

Azimuthal angles of $90 \pm 5^\circ$ and $270 \pm 5^\circ$ give the strain along the loading direction, longitudinal strain, and $0 \pm 5^\circ$ and $180 \pm 5^\circ$ give the transverse strain.

In the case of the SAXS patterns the peaks arise from the ~ 67 nm periodic spacing of the mineralized collagen fibrils. Changes in the measured SAXS spacing with applied load therefore represent changes in the average HAP platelet spacing, which in turn results from cooperative deformation between the collagen and HAP platelets. Thus, the SAXS-derived strain provides the composite response on the nanoscale level (without the effects from the larger microstructure such as Haversian canals and tubules), and is therefore described as the fibrillar strain. Measurement of this fibrillar strain is similar to the HAP elastic strain measurements except that the third-order SAXS peak is used and that a strain-free point, R^* , is not measured. Instead, the strain-free point is taken to be the radial distance, $R(\eta)$, of the rings when the sample is under zero load. For the mineralized fibrils, transverse strains are difficult to determine due to low diffraction intensities at the $0 \pm 10^\circ$ and $180 \pm 10^\circ$ azimuths.

For the static creep experiments, the obtained strains are plotted versus time with the slope of the plots representing the steady-state creep strain rate, which represents the rate at which the HAP or mineralized fibrils accumulate or shed strain during static loading. For the unload/load segments of the interval creep measurements, the HAP and fibrillar strains are plotted as a function of applied stress. The slopes of these plots are defined as the apparent modulus ($E_{app} = \sigma_{applied} / \varepsilon_{phase}$)

which provides information about how load is transferred between the phases.

2.3.2. Peak broadening analysis

Radial peak broadening (ΔR_{meas}) can result from strain distributions within the sampled population, the small size of the HAP platelets, as well as instrumental effects. The instrumental contribution for the HAP (00.2) and HAP (00.4) peaks was calculated using the ceria standard. Using the pseudo-Voigt fit of the diffraction peaks, the instrumentally-corrected mineral peak width (ΔR) was converted to $\Delta 2\theta$ using $\Delta 2\theta = \Delta R/z$, where z is the sample to detector distance. From known values for the HAP (00.2) and HAP (00.4) angular peak widths ($\Delta 2\theta$), the crystallite size (D) and root mean square strain (ε_{rms}) can be calculated from the following equation (Noyan and Cohen, 1956):

$$\Delta 2\theta \cos \theta = \frac{180}{\pi} \left[\frac{\lambda}{D} + 2 \left\langle \left(\frac{\Delta d}{d} \right)^2 \right\rangle^{1/2} \sin \theta \right] \quad (2)$$

where $\langle x \rangle$ denotes the mean of x , λ is the X-ray wavelength, and ε_{rms} is represented by $\langle (\frac{\Delta d}{d})^2 \rangle^{1/2}$. The root mean strain, ε_{rms} , represents the variation in strains within the sampling volume (Almer and Stock, 2005, 2007).

2.3.3. Peak intensity analysis

The variation in intensity along the azimuthal direction of the diffraction rings is due to preferential alignment of the HAP platelets, i.e., to texture. To determine how the orientation of the HAP platelets might change with continuing creep, the normalized intensity of the HAP (00.2) peak was plotted as a function of azimuth. A non-textured material would show a constant intensity at all azimuths while a textured material would show peaks in intensity at azimuthal angles associated with the preferred diffractor orientation. Changes in the distribution of intensity with time during creep were determined by measuring the azimuthal full-width-half-max (FWHM) of the high intensity peaks, measured at 90° and 270° for the HAP (00.2) diffraction peaks in the bone and dentin samples, as a function of time. An increase in the intensity peak FWHM represents a tilting of the platelets away from the preferential orientation and vice-versa.

2.4. Finite element modeling

To elucidate the effect of irradiation on the deformation mechanisms of bone and dentin at high X-ray radiation dosage, a number of 2-D FEM models of the mineralized collagen fibril were created using the software ABAQUS 6.10-EF1. Since the microstructure for both bone and dentin at this level is similar (Weiner and Wagner, 1998), the same geometry is used here for both. The basic geometry of the models is based on a previous model used to simulate the elastic and creep properties of the bone collagen fibril at low X-ray dosage conditions (Yuan et al., 2010), modified from the original proposal by Jager and Fratzl (2000). In the original model, the fibrillar structure including the 67 nm period of the collagen assembly (Ten Cate, 1980) and the overlapping distribution of parallel intra-fibrillar HAP platelets in the axial direction were addressed. However, this model ignored

interfacial interactions at the collagen–collagen and HAP–collagen interfaces which are important for modeling damage.

Using the geometry described by Jäger and Fratzl as a starting point, model 1 was created by adding HAP–collagen interfacial forces and smoothing the HAP–collagen intersections to avoid stress concentrations (Fig. 2a). To simulate the HAP–collagen interfacial debonding/rebonding behavior hypothesized for the radiation tests, a friction law was applied to the HAP–collagen interface. This friction assumption is such that when the shear force on the interface is small, no sliding between the phases is allowed due to the static friction, simulating a fully bonded interface; however, when the shear force is above a critical value, sliding is initiated, simulating broken interfacial bonds. Furthermore, when the shear force returns to a low value, the sliding ceases and the static friction condition is restored. These three steps represent the bonding–debonding–rebonding behaviors of the HAP–collagen interface.

In model 1, the collagen matrix was also assumed to be continuous, with a bulk Young’s modulus of 5 GPa (as measured ultrasonically (Chapel’ and Lavrent’ev, 1987)) and Poisson’s ratio of 0.25 (Meyers et al., 2008). The HAP platelets have an aspect ratio of 26.8, a bulk Young’s modulus of 114 GPa and Poisson’s ratio of 0.28 (Gilmore and Katz, 1982). An empirical equation proposed by Sasaki et al. (1999) was used to represent the viscoelastic properties of the collagen phase:

$$E(t) = E_0\{A_1 \exp[-(t/\tau_1)^\beta] + A_2 \exp(-t/\tau_2)\} \quad (3)$$

where E_0 is the modulus at $t=0$, τ_1 and τ_2 are two relaxation times, β is the stretched exponential parameter which effectively spreads the relaxation time τ_1 over a larger range, and A_1 and A_2 are the weighting fractions of the two terms. In this expression, $0 < \beta \leq 1$ and $A_1 + A_2 = 1$. Based on our previous study on bone collagen fibril under low X-ray dosage conditions (Deymier-Black et al., 2012a), the parameters were set as $\tau_1 = 100$ s, $\tau_2 = 10^5$ s, $\beta = 1$ and $A_1/A_2 = 6$ (Deymier-Black et al., 2012a). By using the above parameters, the collagen modulus at long times (in the mechanical measurement range) is about 1 GPa, which is the commonly accepted value (Meyers et al., 2008). Model 1 provides important information about the effect of interfacial strengths on fibrillar mechanics but in its assumption that the collagen is a continuous visco-elastic matrix, it overlooks the true structure of collagen.

The collagen matrix is composed of assemblies of discrete triple-helix molecules, which are about 300 nm in length and 1.5 nm in diameter (Orgel et al., 2001). Because the 300 nm length of the individual collagen molecule is significantly larger than both the assembly period (67 nm) and the HAP platelet (mostly < 100 nm long in axial direction), the collagen fibers are unlikely to terminate exactly at the extremities of the mineral plates (surface BC in Fig. 2b). Therefore, a second model, model 2, was created such that the continuous collagen matrix in the model 1 (Fig. 2a) is discretized into several adjacent long collagen regions, corresponding to individual collagen fibers (Fig. 2b). This long fiber morphology and the platelet-like shape of mineral result necessarily in a region (region BCE) in which materials can take large deformation but with little stress concentration. This region is assumed to be highly hydrated and is modeled as a non-load bearing interstitial space or void. This new geometry requires

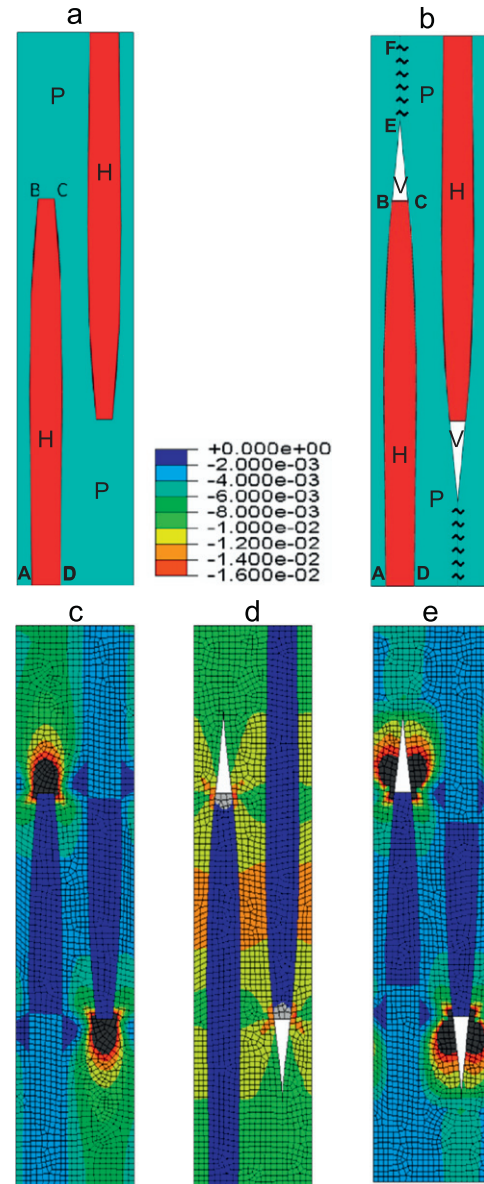


Fig. 2 – Schematics of the 2-D mineralized collagen fibril FEM models for (a) the model with the continuous collagen phase and (b) the model with the consideration of discreteness of collagen phase. Areas labeled H are HAP, P are Protein (collagen), and V are the voids. Labels A-F are used to provide reference points in the model, i.e., Segment EF represents the collagen–collagen interface. Also shown are the FE meshes and simulated strain distribution (strain values in dimensionless units are given in color scale) at the final creep loading state for (c) the model with a continuous collagen phase and interfacial sliding, (d) the model with the consideration of discreteness of collagen phase with interfacial debonding/rebonding and (e) the model with consideration of discreteness of the collagen fibers but without the interfacial debonding/rebonding. Gray regions represent nodes under tensile strains. (For interpretation of the references to color in this figure legend, the reader is referred to the web version of this article.)

consideration of the collagen–collagen interfacial behavior. To simplify the calculation, only the collagen–collagen interfaces directly influencing the transfer of load, or load

Table 1 – Parameters used in the FEM simulation.

	Model geometry		Elastic properties			Friction		Spring stiffness (MPa)
	Length (nm)	Width (nm)	Young's modulus (GPa)	Poisson's ratio		Friction coefficient	Shear stress limit (MPa)	
HAP	46.9 ^a	3.5 ^b	114 ^c	0.28 ^c	HAP–collagen	0.5	100	–
Collagen	67 ^b	4 × 3.5 ^b	5 ^d	0.25 ^d	Collagen–collagen	–	–	3 ^e

^a Ascenzi, A., et al., *Journal of Ultrastructure Research* 12, 287–&.
^b Lowenstam, H.A., et al., 1989.
^c Gilmore, R.S., et al., *Journal of Materials Science* 17, 1131–1141.
^d Chapel', V., et al., *Mechanics of Composite Materials* 14, 574–579.
^e Deymier-Black, A.C., et al., *Acta Biomaterialia* 8, 253–261.
^f The length of the HAP platelets in the model is a half of the length of a natural platelet due to symmetry used in the model.

transfer, between HAP and collagen phases, i.e., those directly above or below the platelets were considered. Above/below the void, the collagen–collagen interface (along EF in Fig. 2b) was modeled as connected with springs added between the corresponding nodes on the neighboring collagen fiber regions to simulate the interaction forces. The stiffness of the springs is taken as 3 MPa, as reported in Deymier-Black et al. (2012a) for the stiffness of the crosslinks. All other parameters were kept the same as in model 1 and are listed in Table 1.

To accurately determine the role of interfacial debonding during the creep loading, a third model, model 3, was created as a control. Model 3 uses the same interstitial geometry as model 2 but ignores the HAP–collagen debonding. Instead the HAP–collagen interface was modelled as being fully bonded, forcing any two neighboring nodes to deform together under load. In comparison to models 1 and 2, model 3 serves to deconvolute the effect of the interstitial space and the interfacial effect.

For all three models, the unit cell was meshed by using linear elements and the model was solved via the ABAQUS standard scheme (sample meshes are shown in Fig. 2c–e). The experimental conditions (–95 MPa constant compressive stress for 3 h) were input into the FE models to replicate the experimental results. The average HAP strain was calculated as the average strain over all the elements in the whole HAP platelet volume; the fibrillar strain was calculated as the displacement of the top of the unit cell divided by the cell height of 67 nm (Deymier-Black et al., 2012a; Yuan et al., 2010).

3. Results

3.1. Static creep

The bone and dentin samples show very similar trends for static creep experiments, as shown in Fig. 3a and b. The residual elastic strain in the HAP platelets before the application of load is $-1020 \pm 40 \mu\epsilon$ for the dentin and $-1960 \pm 45 \mu\epsilon$ for the bone (hollow symbols in Fig. 3a and b). The initial residual strain for the mineralized fibrils is defined as zero. Immediately upon loading to –95 MPa, strong compressive

strains are measured: -4630 ± 56 and $-4110 \pm 1060 \mu\epsilon$ for bone HAP and the mineralized fibrils, and -4200 ± 36 and $-5500 \pm 550 \mu\epsilon$ for the two measurements in dentin (first solid points in Fig. 3a and b). However, with increasing time under static load, the elastic HAP strain decreases and the fibrillar strain increases. In the case of dentin, the strain rate on either phase is near linear with values of $-19.9 \pm 0.9 \mu\epsilon/\text{min}$ for the mineralized fibrils and $7.0 \pm 0.3 \mu\epsilon/\text{min}$ for HAP. Bone exhibits changes in strain in the first 2.5 h of loading followed by a near plateau. The highest strain rates for the bone sample are $-23 \pm 2 \mu\epsilon/\text{min}$ for the mineralized fibrils, measured between 10 and 108 min, and $17.0 \pm 0.5 \mu\epsilon/\text{min}$ for HAP, measured between 40 and 117 min.

Model 1 (Fig. 2a), does not match the experimental results regardless of the parameter values chosen for friction coefficient and shear stress limit, which control the debonding and rebonding behavior (solid lines in Fig. 3c). Although the fibrillar strain is found to increase as measured experimentally (Fig. 3a and b), the HAP strain in Fig. 3c also increases with time at a rate of $-0.12 \mu\epsilon/\text{min}$. Debonding occurred at the interface between the HAP and the collagen along the sides of the platelet (AB and CD in Fig. 2a), thus partially removing load on the platelets; however, this release is compensated by the load transferred to the platelet by the collagen matrix at the BC interface: as shown in Fig. 2c where the maximal longitudinal strain is located near the two tips of the HAP platelets. Model 3, which considers discrete collagen fibers without sliding at the HAP–collagen interface, exhibits results similar to model 1 (Fig. 3c dotted lines) with the HAP strain increasing at a rate of $-0.14 \mu\epsilon/\text{min}$. Here the opposite loading trend is occurring; even in the presence of interstitial spaces, the compressive load is transferred from the collagen to the mineral phase by shear forces during creep (Fig. 2e). Therefore, compressive strain in the mineral phase continues to accumulate with time under constant creep stress.

In the model 2, which accounts for both the discreteness of collagen and the frictional debonding–rebonding of the HAP–collagen interface, the trends in the evolution of fibrillar and HAP strains (Fig. 3d) are in agreement with the experimental results (Fig. 3a and b). Upon application of the initial applied load, both phases accumulate compressive strains of -1357 and $-4979 \mu\epsilon$ for the HAP and mineralized fibril, respectively. The HAP value is lower than the

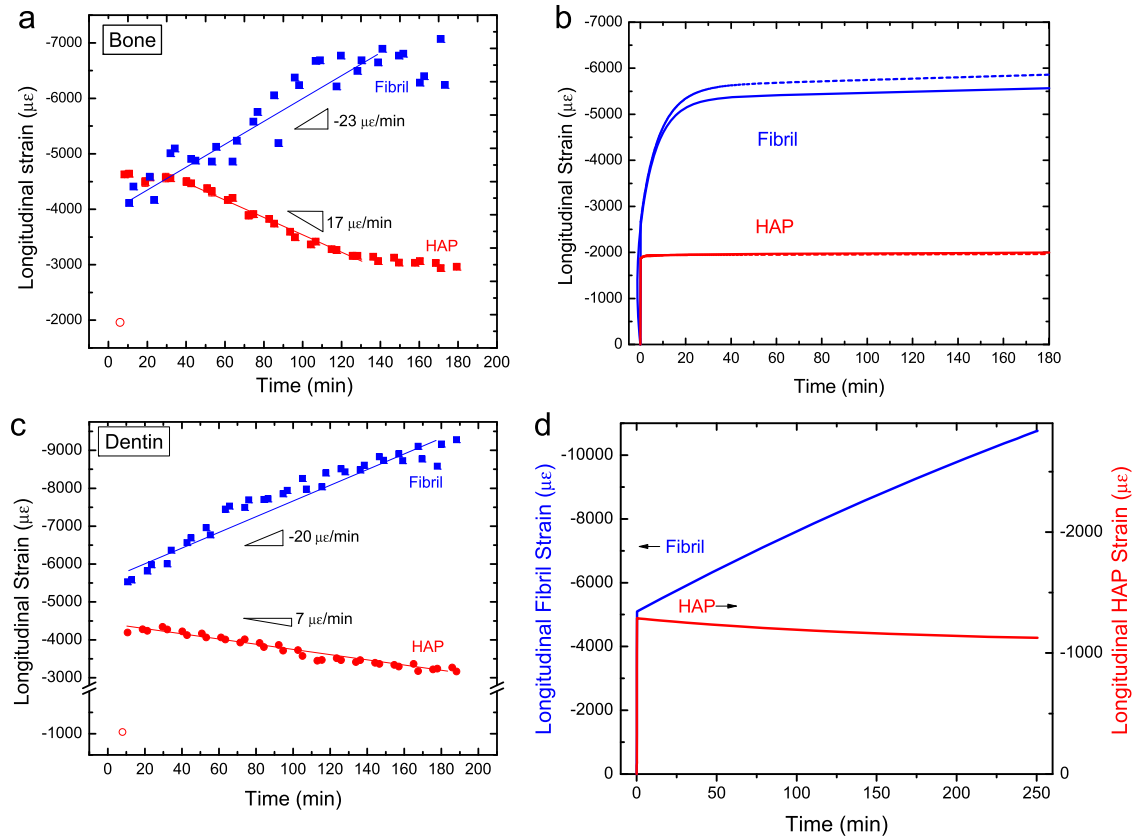


Fig. 3 – Examples of experimental and simulated static creep data. Experimental results are shown for samples of (a) bone and (c) dentin held at a stress of -95 MPa for 3 h. The hollow symbols are the HAP residual strain before application of load. Results from the FEM simulation are shown in (c) for the model 1 with the continuous collagen phase and debonding (solid curves) (Fig. 2a) and model 3 with interstitial spaces and no debonding (dashed curves), as well as in (d) for model 2 with the consideration of discreteness of collagen phase and debonding. Average standard deviations on each point are 48 and 815 $\mu\epsilon$ for the HAP and fibril, respectively.

experimental value in part because the models do not account for initial residual strains. Then, as creep proceeds, the fibrillar strain increases while the HAP strain decreases. The simulated strain rates for the HAP and the mineralized fibril are 0.60 and -15.19 $\mu\epsilon/\text{min}$, respectively. Compared to the model 1, without the interstitial phase (Fig. 2c), small tensile longitudinal strains appear at the tip of the HAP platelets even though the load is compressive (gray colored region in Fig. 2d). Since model 2 is the only one able to reproduce the static creep results, it is used in the following to model the interval creep experimental results.

3.2. Interval creep

The interval creep experiments allow for three measurements of the apparent elastic moduli of the two phases after 1, 2, and 3 cycles/h of creep. As illustrated in Fig. 4a and b, the bone and dentin samples show the same creep trends in the interval creep experiments, as in the static creep experiments: the HAP strain of both samples decreases with loading time, while the fibrillar strain increases with time. However, in this measurement the dentin creep also shows a higher strain rate in the first hour of creep followed by a significantly lower strain rate. For both bone and dentin, the apparent elastic moduli ($E_{app}^{phase} = \sigma_{applied} / \epsilon_{phase}$),

measured by taking a best fit of the slopes in the unload/load segments of the curves for both HAP (E_{app}^{HAP}) and the mineralized fibrils (E_{app}^{Fib}), were within experimental error of each other after one, two or three cycles of creep (Fig. 5a). The average E_{app}^{HAP} and E_{app}^{Fib} , reported as mean \pm standard deviation from the best fit, for bone calculated from the three load and unload curves are 41 ± 3 and 13 ± 1 GPa, respectively. For dentin, average E_{app} of 32 ± 3 and 11.4 ± 0.6 GPa were measured for HAP and mineralized fibrils. These values agree with E_{app}^{fib} values of 16 ± 5 GPa found in dentin (Deymier-Black et al., 2012b) and 16 ± 4 GPa found in bovine bone (Singhal et al., 2011), but are slightly higher than the values of ~ 10 and 6.0 GPa found for bovine bone using similar techniques in compression (Akhtar et al., 2008a) and tension (Gupta et al., 2005). The E_{app}^{HAP} values measured here are higher than previously reported values of 27 ± 7 , 26 ± 6 , ~ 21 GPa for bovine dentin (Deymier-Black et al., 2012b), bovine bone (Singhal et al., 2011), and fallow deer antler (Akhtar et al., 2008b), but on the order of the 38.2 GPa measured for canine fibula (Almer and Stock, 2007).

The FE model, also exhibited no change in the elastic modulus of bone or dentin after 1, 2, or 3 h of creep. The average values of simulated apparent elastic modulus are 38.0 ± 0.8 GPa for the HAP. The simulated fibril modulus is difficult to determine since the unloading and loading slopes are not linear but composed of two linear sections.

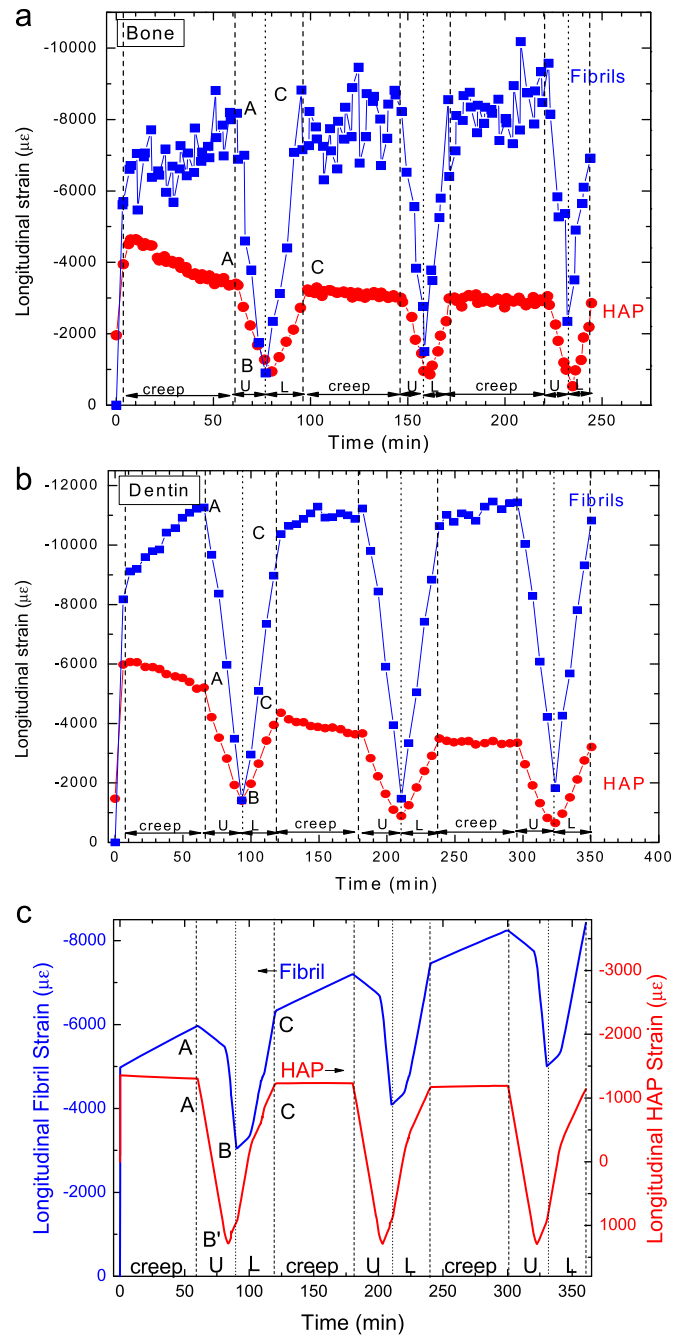


Fig. 4 – Example of creep with load and unload at 1 h intervals for (a) bone and (b) dentin held at -95 MPa. Simulation results are shown in (c). Loading regions of creep, unloading (U), and loading (L) are delimited by dashed and dotted lines. The applied load at point B and along all the other dotted lines is 0 MPa and therefore the strains are residual strains. Points A and C represent the beginning of unloading and the end of loading at which the applied load is -95 MPa. Average standard deviations on each point are 44 and 735 $\mu\epsilon$ for the HAP and fibril, respectively.

In dentin, there is a discontinuity in the creep behavior before and after the unload/load segment for both the HAP and fibrillar strains (Fig. 4b). The strain in the HAP and the mineralized fibrils is larger before the unload/load segment (Fig. 4b, Point A), than it is after the unload/load segment (Fig. 4b, Point C), although the applied stress (-95 MPa) is the same. For the mineralized fibrils, this is true for all three unload/load segments; for the HAP, the discontinuity is most pronounced in the first unload/load segment

(840 $\mu\epsilon$), and small in the 2nd (160 $\mu\epsilon$) and 3rd (150 $\mu\epsilon$). In bone (Fig. 4a), the noisiness of the fibrillar data makes it impossible to determine whether this discontinuity exists. The bone HAP strains show a small discontinuity (120 $\mu\epsilon$) for the first unload/load segment but the discontinuities in the second and third are within experimental error. The magnitude of the HAP strain discontinuities in the model decreases with increasing number of unload/load segments from 85 to 60 and finally to 37 $\mu\epsilon$ (Fig. 4c). The

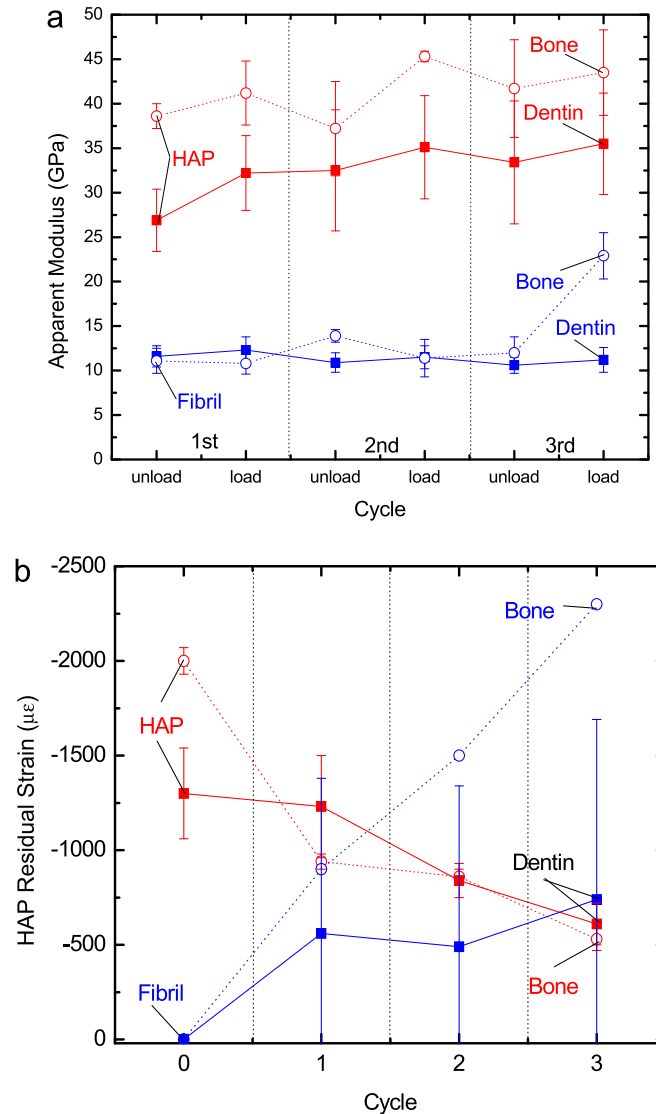


Fig. 5 – Variation of (a) the apparent moduli and (b) residual strain of HAP (shown in red) and the fibrils (shown in blue) in dentin (■) and bone (○) with cyclic loading and unloading. The error bars for the apparent moduli are the standard deviations from the best fit line. The error bars for the residual strain are standard deviations from the mean for the three measured points in the case of dentin and standard deviations from the best fit of strain in the case of bone which only has one measured point. (For interpretation of the references to color in this figure legend, the reader is referred to the web version of this article.)

magnitude of the discontinuities in the simulated results are lower than those measured in dentin experimentally (840–150 μϵ) but are on the order of those measured in the bone (120–35 μϵ).

The residual strain, measured at zero stress after full unload in each of the three unload/load segments (Fig. 4, Point B for the first segment), also evolved with continued creep. As seen in Fig. 5a and b, for both the bone and dentin samples, the residual strain increases with each unload/load segment in the case of the mineralized fibrils and decreases for the HAP. Similarly, in the model, the residual strains in the mineralized fibril increase with each subsequent unloading and slightly decrease for the mineral phase (Fig. 4c). In the model, however, the average strain of the platelets becomes positive (i.e., tensile) during unloading and the maximal

tensile strain (point B') in the mineral phase appears ahead of the zero load point (point B).

3.3. Peak broadening

WAXS peak broadening analysis provides information about the size and distribution of strain within and between the HAP platelets in the sampling volume. The longitudinal size of the HAP platelets was found, using Eq. (2), to be 71 ± 1 and 50 ± 8 nm for bone and dentin static creep samples, respectively, as averaged over the entire creep time (3 h). These values are in agreement with the sizes of 30–60 nm usually found with TEM and X-ray diffraction (Ziv and Weiner, 1994). The longitudinal HAP size shows neither a decreasing nor increasing trend with increasing creep time. The longitudinal RMS strain, however, did

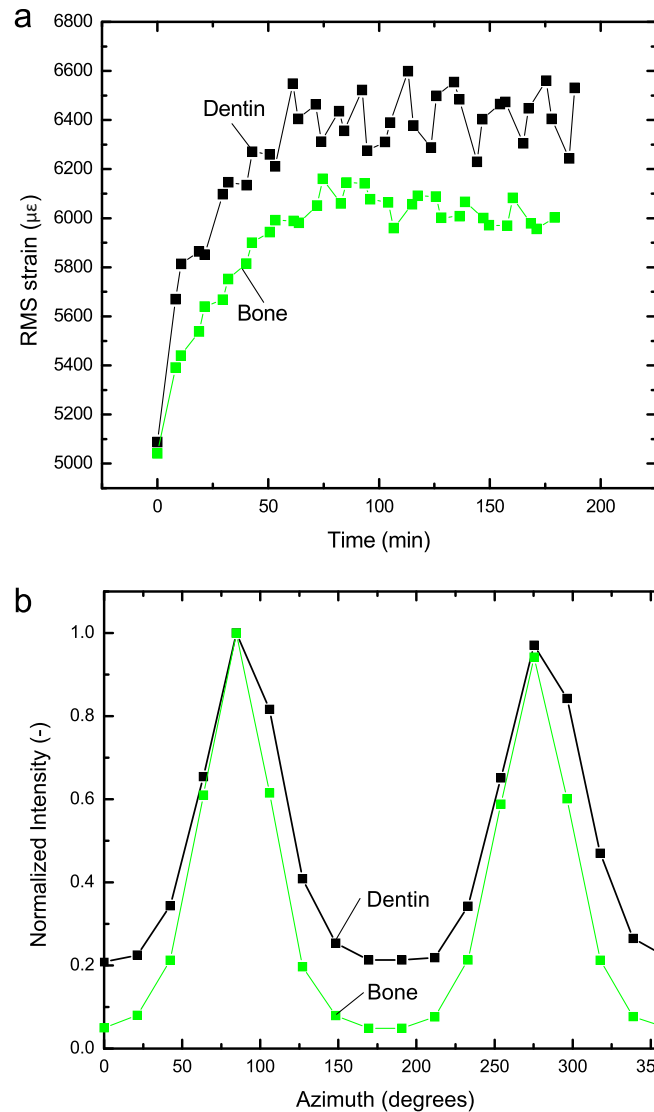


Fig. 6 – (a) ϵ_{RMS} for bone and dentin as a function of creep at -95 MPa. (b) Plot of intensity as a function of azimuth for dentin and bone samples before loading. The intensity is highest about 90° and 270° for both bone and dentin suggesting a preferential alignment of HAP platelets along the longitudinal axis.

not remain constant with creep time in either type of sample, as shown in Fig. 6a. In both dentin and bone, the RMS strain increased steadily during the first hour of loading and remained constant for the following 2 h. In bone, the longitudinal RMS strain increased by $950 \mu\epsilon$, from 5090 to $6550 \mu\epsilon$ (15% increase), and in dentin by $1460 \mu\epsilon$, from 5040 to $5990 \mu\epsilon$ (22% increase).

3.4. Peak intensity

The azimuthal intensity of the HAP (00.2) diffraction ring varied strongly (by 80% for dentin and 95% for bone between the maximum and minimum values) for both the unloaded dentin and bone samples before creep, with peak intensities being highest around the 90° and 270° orientations and lowest at the 0° and 180° orientations (Fig. 6b). This is in agreement with other literature sources for bone and dentin (Stock et al., 2011; Wenk and Heidelbach, 1999). The average FWHM of the peak intensities for the (00.2) reflection was larger for the dentin samples (58°) than for the bone samples

(50°) which are more textured, as illustrated in Fig. 6b. However, in both cases, the FWHM of the (00.2) intensity distribution increases by 2° with initial loading, before stabilizing and becoming constant at this value. In dentin, this change in FWHM upon loading occurs within the first 10 min after loading. However, in bone, the increase in FWHM stretches over the first hour after initial loading before stabilizing.

4. Discussion

At a stress of -95 MPa, the bone and dentin samples are loaded well below their respective yield stresses of -196 (Cowin, 1989) and -160 MPa (Craig and Peyton, 1958; Peyton et al., 1952). Therefore, immediately upon loading, the bone and dentin deform elastically, resulting in elastic stresses (and strains) in the HAP phase and the mineralized fibril. For bone, immediately upon loading (i.e., after 3 min), the elastic

fibrillar strain (first point in Fig. 3a), which represents the nano-scale composite strain at the level of the fibrils, is lower than the elastic HAP strain (first point in Fig. 3a). This is unexpected because the fibril is a HAP-collagen composite and therefore should be more compliant than the HAP itself. The strain on the mineralized fibril upon loading to -95 MPa in this bone sample (Fig. 3a) is significantly lower ($4110 \mu\epsilon$) than in Figs. 3b and 4a and b ($6370 \pm 1410 \mu\epsilon$), suggesting that the fibrillar strain is abnormally low. Since all of the fibrillar strains are measured in relation to the strain at zero stress, errors in the SAXS measurements are easily propagated. Therefore, the fibrillar strains have larger errors in their absolute values, but the trends of the fibrillar strains are very reliable and consistent.

As found in bone samples at low irradiation doses (Deymier-Black et al., 2012a), the fibrillar strain increased

with advancing creep time; however, the HAP strain decreased (Figs. 3 and 4a and b). This is unexpected, as for discontinuously reinforced composites such as bone and dentin, increasing load should be transferred from the compliant, deforming matrix to the stiffer, elastic reinforcement phase with advancing creep time, causing an increased elastic strain in the reinforcement (Daymond et al., 1999). The measured decrease in strain on the HAP reinforcement, as seen in Figs. 3 and 4a and b, may occur due to a number of effects. Three possible hypotheses are (i) the presence of a bimodal strain distribution between that intra-fibrillar and extra-fibrillar HAP, (ii) tilting of the HAP platelets along a preferentially load-bearing direction, and (iii) interfacial delamination between the collagen and the HAP platelets.

The first hypothesis is based on the fact that the HAP platelets in dentin and bone are known to fall into two

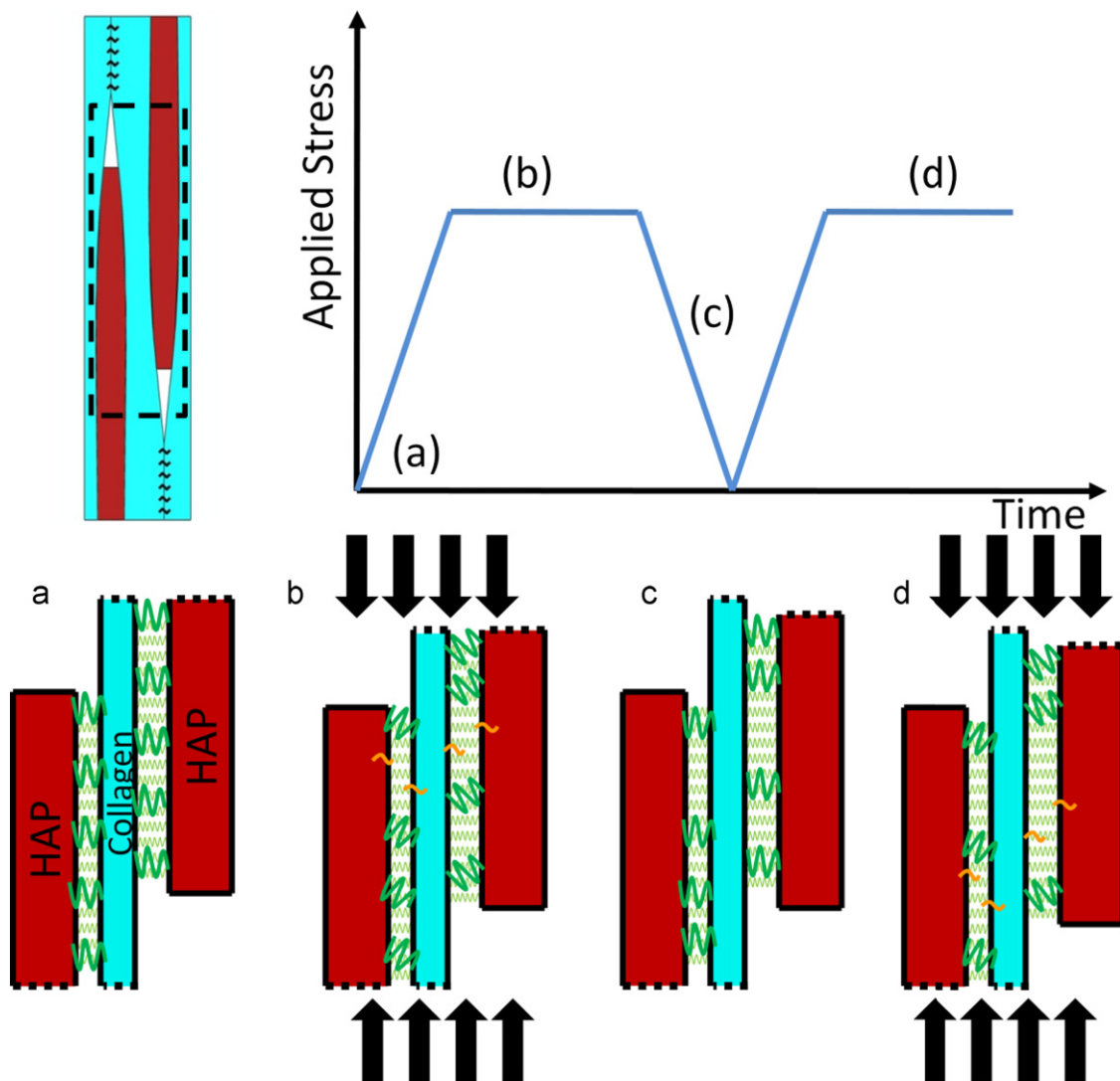


Fig. 7 – Schematic showing the evolution of damage at the HAP-collagen interface in the mineral overlap zone. (a) Initial state of the interface before loading or irradiation with carboxyl bonds (thick green wavy connectors) and reversible bonds (small light-green wavy connectors); (b) HAP-collagen interface damage due to irradiation of carboxyl bonds (orange broken bonds) as well as the high constant stress (tilted carboxyl bonds); (c) rebonding upon unloading with bonds being formed at different locations than before due to the sliding of collagen molecules; (d) Interfacial damage on reloading due to creep stress and irradiation. (For interpretation of the references to color in this figure legend, the reader is referred to the web version of this article.)

separate populations: intra-fibrillar and extra-fibrillar HAP (Bonar et al., 1985; Katz and Li, 1973; Kinney et al., 2003). It is possible that their different locations within the hierarchy of these mineralized biological materials could cause differences in their strain evolution during creep. Therefore, the measured decrease in average HAP strain might actually be caused by a bi-modal strain distribution with a large decrease in strain on the extra-fibrillar HAP, due to fibrillar sliding for example (Gupta et al., 2005), overwhelming a small increase in strain on the intra-fibrillar HAP population. If this were true, the RMS strain, which represents the distribution of strain within the HAP in the sampling volume, would continually increase with creep as the HAP strain decreases. Such an increase is not consistently seen from the broadening analysis (Fig. 6a), eliminating a bi-modal strain distribution as a primary explanation.

The second hypothesis, tilting of the platelets towards a preferentially load-bearing direction, the long-axis which is parallel to the applied load, could also cause a decrease in the measured HAP strain. However, the intensity analysis results show that, upon applying a compressive stress, the HAP platelets tilt away from the longitudinal direction. This should cause an increase in the measured HAP strain in this sub-population of platelets. Tilting is therefore not a valid explanation for the decrease in HAP strain with increasing creep time.

The third hypothesis for the decrease in HAP strain with creep is the presence of damage at the HAP–collagen interface. The HAP–collagen interface, which is maintained by calcium-mediated ionic bonds, hydrogen bonds, Van der Waals forces and water surface tension (Walsh and Guzelsu, 1994; Walsh et al., 1994; Luo et al., 2011), Fig. 7(a), likely undergoes sliding processes during loading, dissipating energy by increasing the collagen deformation and transferring load to the HAP reinforcement (Ji and Gao, 2010). This transfer of load from the collagen to the reinforcement is seen during creep of unirradiated bone (Deymier-Black et al., 2012a). However, in this study as well as in investigations of residual strain evolution in irradiated bone (Singhal et al., 2011) the behavior has been reversed with the HAP reinforcement shedding load to the collagen. In non-biological composites, it has been observed that as debonding of the matrix–reinforcement interface occurs, the capability of the matrix to transfer load to the reinforcement decreases; thus, the matrix stress and elastic strain increases while those for the reinforcement decreases (Schobel et al., 2011). This suggests that the HAP strain decrease may be a result of HAP–collagen interfacial damage.

Hubner et al. (2005), theorized that the interfacial bond damage caused by irradiation is a result of decarboxylation of the collagen side chains, which form calcium-mediated bonds with the HAP surface phosphate groups, and may act as sacrificial bonds in unirradiated bone (Thompson et al., 2001). The loss of carboxylated side-chains decreases the number of possible interfacial bonds between the HAP and the mineralized collagen fibril, thus weakening the interface and limiting the ability of collagen to transfer load. The collagen may also undergo increased crosslinking during irradiation which would decrease its fracture energy (Barth et al., 2011). Such a decrease in fracture energy of the collagen has been shown to result in increased interfacial cracking (Ji

and Gao, 2010). Progressive interfacial damage due to debonding or cracking decreases the efficiency of load transfer, resulting in a continued loss of the HAP elastic strains during creep (Fig. 7(b) and (d)).

This damage hypothesis is supported by the FE model which requires incorporation of HAP–collagen interfacial delamination in model 2 to match the trends of the experimental results. Interestingly, when comparing the simulation results, the maximal longitudinal strain in model 3, without debonding, is much larger ($-57,668 \mu\epsilon = -0.58\%$, Fig. 2e) than in models 1 and 2 that included debonding: -0.32% (model 1 without interstitial spaces, Fig. 2c) and -0.14% (model 2 with interstitial spaces, Fig. 2d). This suggests that HAP–collagen interfacial debonding serves as a mechanism for the redistribution of strains in bone, lowering the maximal strain in the collagen phase.

However, the strain rate ($0.55 \mu\epsilon/\text{min}$) from simulation is much lower than the experimental results ($\sim 7 \pm 0.3 \mu\epsilon/\text{min}$ for dentin and $17 \pm 0.5 \mu\epsilon/\text{min}$ for bone). The reason for this discrepancy is likely due to oversimplification of the current model. Although our previous simulation showed that the elastic properties based on 2D and 3D models are similar (Yuan et al., 2010), this may not hold, for the creep behavior. Furthermore, at least two major assumptions can contribute to this difference. The first is associated with the hierarchical structure of bone and dentin. In the current model, only the mineralized collagen fibril level is considered, which ignores the presence of extra-fibrillar mineral platelets between collagen fibrils (Katz and Li, 1973). As mentioned earlier, the influence of these extra-fibrillar mineral on the strain evolution is indistinguishable from the intra-fibrillar mineral, but the existence of extra-fibrillar mineral platelets may change the overall magnitude of the strain in the HAP phase. Moving further up in the bone and dentin hierarchy, multiscale modeling studies show that the existence of Haversian canals, tubules, and macroscopic pores in bone and dentin also affect the elastic strain at the mineralized collagen fibril level (Hamed et al., 2010, 2012) and therefore probably the creep strain; however, no detailed data are available due to difficulties in measuring viscoelastic and interfacial properties of various individual phases, such as non-collagen proteins (Cowin, 2001). Second, the parameters used to represent the viscoelastic properties of the collagen phase are difficult to define. The parameters used here are deduced from very similar creep measurements on bone but at low X-ray dosage levels (Deymier-Black et al., 2012a). As previously mentioned, the high-energy X-ray irradiation can cause changes in the collagen properties (Nguyen et al., 2007a; Dziedzic-Goclawska et al., 2005; Barth et al., 2010). Therefore, the two modes of relaxation and the ratio between them may also be altered, which would also contribute to the inaccuracy of the strain magnitude.

The changes in residual strains (strains measured at zero stress) in the interval creep experiments (Fig. 4a and b, point B for the first unload/load segment) are also evidence that delamination may be occurring. In the case of the fibrillar strain, an increase in the residual strain would be expected with repeated loading cycles due to viscoelastic and/or plastic deformation through molecular sliding (Ji and Gao, 2010). This inelastic deformation results in compressive strains

being present in the mineralized fibrils even after complete unloading (Fig. 4a and b, point B for the first unload/load segment). On the other hand, the initial residual HAP strains decrease with continued creep and irradiation (Fig. 5b). As discussed elsewhere (Singhal et al., 2011), irradiation causes a decrease in HAP residual strain as a result of HAP platelet relaxation during interfacial debonding, thus releasing the initial residual strains.

The trend of residual strain increasing in collagen and slightly decreasing in HAP is also seen in the FE model (Fig. 4c). However, in this case the HAP strain becomes tensile at low loads. The presence of tensile residual strains in the mineral phase is probably due to the ability of collagen to both elastically deform and slide. As mineralized fibrils are unloaded past the critical debonding/rebonding stress, the HAP–collagen interface reforms. This is seen by the change in fibrillar modulus in Fig. 4. However, as unloading continues, the collagen fibers continue to relax. As the fibers expand from a compressive strain state, they pull on the HAP–collagen interfaces, applying tensile stresses to the mineral. Eventually, the tensile stress applied to the mineral during the continued collagen relaxation is high enough that it exceeds the interfacial critical stress. At this point, the tensile stress in the mineral phase is released due to interfacial debonding, even though the zero load point (point B) has not been reached. The fact that such tensile residual stresses are not seen in the experimental diffraction data may be due to the presence of residual compressive strains in HAP in natural bone and dentin before loading which are not considered in the simulation. However, due to the limitation of the current model, it is difficult to introduce a residual strain in the HAP phase without significantly altering the residual strain in the collagen phase and the initial bonding state on the HAP–collagen interface.

With reduced load transfer caused by interfacial delamination, the HAP carries less load and becomes less strained, so the apparent modulus is expected to increase (since the applied stress is constant) with creep time. However, the interval creep experiments (Fig. 4) indicate that the apparent modulus of neither HAP nor the mineralized fibrils changes significantly after one, two or three cycles of creep (Fig. 5a). This lack of change in the apparent modulus values indicates that the extent of load transfer, and therefore bonding/debonding, at the time of the modulus measurement is unchanged. This discrepancy may be resolved, however, by considering the types of interactions at the HAP–collagen interfaces. Although irradiation may affect the Ca-mediated electrostatic bonds, hydrogen bonds, Van der Waals forces and water surface tension (Walsh and Guzelsu, 1994; Walsh et al., 1994; Luo et al., 2011) are also present at the interface (Barth et al., 2010, 2011; Hubner et al., 2005). Many of these bonding forces are reversible in aqueous ion rich environments (Ji and Gao, 2010; Thompson et al., 2001). This suggests that interfacial ‘healing’ may be responsible for the unchanged apparent elastic moduli. According to this explanation, upon unloading, most of the interface, which was previously damaged by irradiation and mechanical loading, will reform reversible bonds allowing the composite to return to its previous stiffness even after extensive delamination (Fig. 7(c)). Modeling work by Luo et al. (2011) has proposed that in order to replicate the diffuse damage seen experimentally in bone, the

interfacial strength would have to be mostly mediated by hydrogen bonds, Van der Waals forces, and water surface tension and not ionic bonds. Additionally, it has been shown that a sub-population of Ca-mediated carboxyl bonds may reform after being broken (Thompson et al., 2001). The FE model, which accounts for both debonding and rebonding of the HAP–collagen interface, is well able to match the experimental results showing both HAP relaxation and a constant HAP modulus.

Previous studies have shown that partial interfacial rebonding is possible after mechanical damage (Singhal et al., 2011; Thompson et al., 2001); however, complete rebonding of the irradiation-damaged bonds is unlikely. This may help explain the elevated values of the HAP apparent moduli ($E_{app}^{HAP} = \sigma_{applied}/\epsilon_{HAP}$), indicating lower strain for a given applied stress, measured in the interval creep experiments (41 ± 3 and 32 ± 3 GPa for bone and dentin) as compared to previous measurements on samples exposed to low doses using the same techniques (26 ± 7 (Singhal et al., 2012) and 27 ± 7 GPa (Deymier-Black et al., 2012b)).

The discontinuities in the HAP and fibrillar strains during creep observed in the experimental and simulation results (Fig. 4, points A and C) before and after the unload/load segment are likely a result of strain recovery. As the sample is unloaded, some of the non-elastic strains in the collagen are also recovered, decreasing the fibrillar strain. This may result from reorientation of the collagen fibrils or entropic reformation of sacrificial bonds (Thompson et al., 2001). Since, the HAP–collagen interface is theorized to reform during unloading, that collagen relaxation will entrain a HAP relaxation.

Finally, in spite of the differences between the simulation and experimental results, the model provides a platform to explore semi-quantitatively mechanisms responsible for bone and dentin deformation under creep loading. The model confirms the viability of the proposed delamination mechanism and can explain the decrease in strain in the mineral phase during the creep. As demonstrated in Fig. 4c, the model shows that rebonding of the mineral–collagen interface during the process of unloading is essential to maintain a relatively constant apparent modulus of bone and dentin. The model also demonstrates the importance of considering the detailed geometry of the collagen matrix: only when the interstitial space in the collagen matrix and the interactions between collagen fibers are considered and combined with the delamination mechanism can the model qualitatively reproduce the experimental results.

5. Conclusions

The load transfer behavior to and from the HAP phase in bovine bone and dentin was studied by in-situ synchrotron X-ray diffraction during creep at 37 °C performed under high stresses (–95 MPa) and large irradiation doses (>650 kGy). Unlike most synthetic composites where load is transferred from the matrix to the reinforcement as creep proceeds, the reinforcing HAP phase in these biological materials sheds some of the load accrued during the initial elastic loading. This decrease in stress (and elastic strain) in the reinforcement suggests that there is interfacial delamination;

however, this is not consistent with the lack of change in the elastic load-sharing behavior of the HAP or the mineralized fibrils during elastic unload/load segments interspersed within the creep experiments. This discrepancy can be explained by a HAP–collagen interface that debonds during long-term creep but rebonds during the intervening elastic unloading–loading segments. The debonding is assumed to occur due to a combination of damage at the interface due to high X-ray irradiation doses and mechanical loading during creep. Rebonding is assumed to take place immediately upon onset of unloading. This debonding/rebonding hypothesis was tested through FE modeling which indicated that not only is delamination required to explain the experimental results but also the presence of a non-load-bearing gap at the ends of the mineral platelets. These results give insights into how biological composites such as bone and dentin behave mechanically at the nanoscale under high stresses and high X-ray irradiation doses, and what role the nanostructure (weak but healing interface, platelet orientation, sliding between collagen molecules, non-load-bearing gaps) plays in such behavior.

Acknowledgments

The authors thank Dr. S.R. Stock (NU) and Dr. Dean R. Haeffner (APS) for numerous useful discussions throughout this work. They also acknowledge Dr. Yu-chen Karen Chen for her help with the experiments at the APS. This research was performed at station 1-ID of APS. Use of the Advanced Photon Source was supported by the U.S. Department of Energy, Office of Science, Office of Basic Energy Sciences, under Contract No. DE-AC02-06CH11357. Partial funding was provided to ACDB by a NDSEG Fellowship from the DOD the NSF Graduate Fellowship.

REFERENCES

- Akhtar, R., et al., 2008H. Load transfer in bovine plexiform bone determined by synchrotron x-ray diffraction. *Journal of Materials Research* 23 (2), 543–550.
- Akhtar, R., et al., 2008b. Elastic strains in antler trabecular bone determined by synchrotron x-ray diffraction. *Acta Biomaterialia* 4, 1677–1687.
- Almer, J.D., Stock, S.R., 2005. Internal Strains and stresses measured in cortical bone via high-energy X-radiation. *Journal of Structural Biology* 152 (1), 14–27.
- Almer, J.D., Stock, S.R., 2007. Micromechanical responses of mineral and collagen phases in bone. *Journal of Structural Biology* 157 (2), 365–370.
- Akkus, O., Belaney, R.M., Das, P., 2005W. Free radical scavenging alleviates the biomechanical impairment of gamma radiation sterilized bone tissue. *Journal of Orthopaedic Research*, 838–84523, 838–845.
- Akhtar, R., et al., 2011. Lattice strains and load partitioning in bovine trabecular bone. *Acta Biomaterialia* 7 (2), 716–723.
- Al-Jawad, M., et al., 2007. 2D mapping of texture and lattice parameters of dental enamel. *Biomaterials*, 2908–291428, 2908–2914.
- Almer, J.D., Stock, S.R., 2010. High energy X-ray scattering quantification of in situ-loading-related strain gradients spanning the dentinoenamel junction (DEJ) in bovine tooth specimens. *Journal of Biomechanics* 43 (12), 2294–2300.
- Barth, H.D., et al., 2010. On the effect of X-ray irradiation on the deformation and fracture behavior of human cortical bone. *Bone* 46 (6), 1475–1485.
- Barth, H.D., et al., 2011. Characterization of the effects of X-ray irradiation on the hierarchical structure and mechanical properties of human cortical bone. *Biomaterials* 32 (34), 8892–8904.
- Bowman, S.M., et al., 1994. Compressive creep-behavior of bovine trabecular bone. *Journal of Biomechanics* 27 (3), 301–310.
- Bolotin, G., et al., 2007. Tissue-disruptive forces during median sternotomy. *Heart Surgery Forum* 10 (6), E487–E492.
- Bonar, L.C., Lees, S., Mook, H.A., 1985. Neutron diffraction studies of collagen in fully mineralized bone. *Journal of Molecular Biology* 181, 265–270.
- Cornu, O., et al., 2000. Effect of freeze-drying and gamma irradiation on the mechanical properties of human cancellous bone. *Journal of Orthopaedic Research* 18 (3), 426–431.
- Currey, J.D., et al., 1997. Effects of ionizing radiation on the mechanical properties of human bone. *Journal of Orthopaedic Research* 15 (1), 111–117.
- Chapel', V., Lavrent'ev, V., 1987. Piezoelectric effect in collagen structures. *Mechanics of Composite Materials* 14 (4), 574–579.
- Cowin, S.C., 1989. *Bone Mechanics*. CRC Press, Boca Raton, FL.
- Craig, R.G., Peyton, F.A., 1958. Elastic and mechanical properties of human dentin. *Journal of Dental Research* 37 (4), 710–719.
- Cowin, S.C., 2001. In: *Bone Mechanics Handbook* second ed. CRC Press, Boca Raton, FL.
- Dziedzic-Goclawska, A., et al., 2005. Irradiation as a safety procedure in tissue banking. *Cell and Tissue Banking* 6, 201–219.
- Deymier-Black, A.C., et al., 2010. Synchrotron X-ray diffraction study of load partitioning during elastic deformation of bovine dentin. *Acta Biomaterialia* 6 (6), 2172–2180.
- Deymier-Black, A.C., et al., 2012a. Evolution of load transfer between hydroxyapatite and collagen during creep deformation of bone. *Acta Biomaterialia* 8 (1), 253–261.
- Deymier-Black, A.C., et al., 2011. Effect of freeze–thaw cycles on load transfer between the biomineral and collagen phases in bovine dentin. *Materials Science and Engineering C* 31 (7), 1423–1428.
- Deymier-Black, A.C., et al., 2012b. Variability in the elastic properties of bovine dentin at multiple length scales. *Journal of the Mechanical Behavior of Biomedical Materials* 5 (1), 71–81.
- Daymond, M., et al., 1999. Elastic phase-strain distribution in a particulate-reinforced metal-matrix composite deforming by slip or creep. *Metallurgical and Materials Transactions A: Physical Metallurgy and Materials Science* 30 (11), 2989–2997.
- El Mowafy, O.M., Watts, D.C., 1986. Fracture toughness of human dentin. *Journal of Dental Research* 65 (5), 677–681.
- Fränzel, W., Gerlach, R., 2009. The irradiation action on human dental tissue by X-rays and electrons—a nanoindenter study. *Zeitschrift für Medizinische Physik* 19 (1), 5–10.
- Gupta, H.S., et al., 2006a. Cooperative deformation of mineral and collagen in bone at the nanoscale. *Proceedings of the National Academy of Sciences of the United States of America* 103 (47), 17741–17746.
- Gupta, H.S., et al., 2006b. Fibrillar level fracture in bone beyond the yield point. *International Journal of Fracture*, 425–436139, 425–436.
- Gupta, H.S., et al., 2005. Nanoscale deformation mechanisms in bone. *Nano Letters* 5 (10), 2108–2111.
- Gilmore, R.S., Katz, J.L., 1982. Elastic properties of apatites. *Journal of Materials Science* 17 (4), 1131–1141.

- Hubner, W., et al., 2005. The influence of x-ray radiation on the mineral-organic matrix interaction of bone tissue: an FT-IR microscopic investigation. *The International Journal of Artificial Organs* 28 (1), 66-73.
- Hamed, E., Lee, Y., Jasiuk, I., 2010. Multiscale modeling of elastic properties of cortical bone. *Acta Mechanica* 213 (1-2), 131-154.
- Hamed, E., et al., 2012. Elastic moduli of untreated, demineralized and deproteinized cortical bone: validation of a theoretical model of bone as an interpenetrating composite material. *Acta Biomaterialia* 8 (3), 1080-1092.
- Jantararat, J., et al., 2002. Time-dependent properties of human root dentin. *Dental Materials* 18 (6), 486-493.
- Jager, I., Fratzl, P., 2000. Mineralized collagen fibrils: a mechanical model with a staggered arrangement of mineral particles. *Biophysical Journal* 79 (4), 1737-1746.
- Ji, B.H., Gao, H.J., 2010. Mechanical principles of biological nanocomposites. In: Clarke, D.R., Ruhle, M., Zok, F. (Eds.), *Annual Review of Materials Research*, vol 40. Annual Reviews, Palo Alto, pp. 77-100.
- Kielbassa, A.M., et al., 2006. Radiation-related damage to dentition. *Lancet Oncology* 7, 326-335.
- Kruzic, J.J., et al., 2003. Crack blunting, crack bridging and resistance-curve fracture mechanics in dentin: effect of hydration. *Biomaterials*, 5209-522124, 5209-5221.
- Kahler, B., Swain, M.V., Moule, A., 2003. Fracture-toughening mechanisms responsible for differences in work to fracture of hydrated and dehydrated dentine. *Journal of Biomechanics*, 229-23736, 229-237.
- Kolovou, P., J. Anastassopoulou, Synchrotron FT-IR spectroscopy of human bones. The effect of aging. In: Tsakanov, V, Wiedemann, H. (Eds.), *Brilliant Light in Life and Material Sciences*, 2007. pp. 267-272.
- Katz, E.P., Li, S.-T., 1973. Structure and function of bone collagen fibrils. *Journal of Molecular Biology* 80, 1-15.
- Kinney, J.H., et al., 2003. The importance of intrafibrillar mineralization of collagen on the mechanical properties of dentin. *Journal of Dental Research* 82 (12), 957-961.
- Luo, Q., et al., 2011. Effect of mineral-collagen interfacial behavior on the microdamage progression in bone using a probabilistic cohesive finite element model. *Journal of the Mechanical Behavior of Biomedical Materials* 4 (7), 943-952.
- Madgwick, A., Mori, T., Withers, P.J., 2002. A neutron diffraction study of creep and damage occurrence in an A359/SiC composite. *Materials Science and Engineering A—Structural Materials Properties Microstructure and Processing* 333 (1-2), 232-238.
- Meyers, M.A., et al., 2008. Biological materials: structure and mechanical properties. *Progress in Materials Science* 53, 1-206.
- Nguyen, H., Morgan, D.A.F., Forwood, M.R., 2007a. Sterilization of allograft bone: effects of gamma irradiation on allograft biology and biomechanics. *Cell Tissue Banking* 8, 93-105.
- Nguyen, H., Morgan, D.A.F., Forwood, M.R., 2007b. Sterilization of allograft bone: is 25 kGy the gold standard for gamma irradiation?. *Cell Tissue Banking* 8, 81-91.
- Nyman, J.S., Reyes, M., Wang, X., 2005. Effect of ultrastructural changes on the toughness of bone. *Micron* 36 (7-8), 566-582.
- Neil Dong, X., Almer, J.D., Wang, X., 2010. Post-yield nanomechanics of human cortical bone in compression using synchrotron X-ray scattering techniques. *Journal of Biomechanics* 44 (4), 676-682.
- Noyan, I.C., Cohen, J.B., 1956. In: Ilschner, B., Grant, N.J. (Eds.), *Residual Stress: Measurement by Diffraction and Interpretation*. Springer-Verlag, New York.
- Orgel, J.P.R.O., et al., 2001. The in situ supermolecular structure of type I collagen. *Structure* 9, 1061-1069.
- Peyton, F.A., Mahler, D.B., Hershenov, B., 1952. Physical properties of dentin. *Journal of Dental Research* 31 (3), 366-370.
- Ritchie, R.O., Buehler, M.J., Hansman, P.K., 2009. Plasticity and toughness in bone. *Physics Today*, 41-47.
- Ritchie, R.O., 2011. The conflicts between strength and toughness. *Nature Materials* 10 (11), 817-822.
- Ren, Y., Maltha, J.C., Kuijpers-Jagtman, A.M., 2003. Optimum force magnitude for orthodontic tooth movement: a systematic literature review. *The Angle Orthodontist* 73 (1), 86-92.
- Singhal, A., et al., 2011A. Effect of high-energy X-ray doses on bone elastic properties and residual strains. *Journal of the Mechanical Behavior of Biomedical Materials* 4 (8), 1774-1786.
- Singhal, A., Almer, J.D., Dunand, D.C., 2012. Variability in the nanoscale deformation of hydroxyapatite during compressive loading in bovine bone. *Acta Biomaterialia* 8 (7), 2747-2758.
- Sasaki, N., et al., 1999M. Time-resolved x-ray diffraction from tendon collagen during creep using synchrotron radiation. *Journal of Biomechanics* 32 (3), 285-292.
- Stock, S.R., et al., 2011. Near tubule and intertubular bovine dentin mapped at the 250 nm level. *Journal of Structural Biology* 176 (2), 203-211.
- Schobel, M., et al., 2011. Thermal fatigue damage in mono-filament reinforced copper for heat sink applications in divertor elements. *Journal of Nuclear Materials* 409 (3), 225-234.
- Thariat, J., et al., 2010. Teeth and irradiation in head and neck cancer. *Cancer/Radiotherapie* 14, 128-136.
- Ten Cate, A.R., 1980. *Oral Histology: Development, Structure and Function*. Mosby, St Louis, MO.
- Thompson, J.B., et al., 2001. Bone indentation recovery time correlates with bond reforming time. *Nature* 414 (6865), 773-776.
- Vashisth, D., 2004. Rising crack-growth-resistance behavior in cortical bone: implications for toughness measurements. *Journal of Biomechanics*, 943-94637, 943-946.
- White, J.M., et al., 1994. Sterilization of teeth by gamma irradiation. *Journal of Dental Research* 73 (9), 1560-1567.
- Wang, X., et al., 2001. The role of collagen in determining bone mechanical properties. *Journal of Orthopaedic Research*, 1021-102619, 1021-1026.
- Winand, H.M.A., Whitehouse, A.F., Withers, P.J., 2000. An investigation of the isothermal creep response of Al-based composites by neutron diffraction. *Materials Science and Engineering A—Structural Materials Properties Microstructure and Processing* 284 (1-2), 103-113.
- Weiner, S., Wagner, H.D., 1998. The material bone: Structure mechanical function relations. *Annual Review of Materials Science* 28, 271-298.
- Wenk, H.R., Heidelberg, F., 1999. Crystal alignment of carbonated apatite in bone and calcified tendon: results from quantitative texture analysis. *Bone* 24 (4), 361-369.
- Walsh, W.R., Guzelsu, N., 1994E. Compressive properties of cortical bone—mineral organic interfacial bonding. *Biomaterials* 15 (2), 137-145.
- Walsh, W.R., Ohno, M., Guzelsu, N., 1994. Bone composite behavior—effects of mineral organic bonding. *Journal of Materials Science—Materials in Medicine* 5 (2), 72-79.
- Yuan, F. A new model to simulate the elastic properties of mineralized collagen fibril. *Biomechanics and Modeling in Mechanobiology* 10 (2), 147-160.
- Ziopoulos, P., Currey, J.D., Hamer, A.J., 1999. The role of collagen in the declining mechanical properties of aging human cortical bone. *Journal of Biomedical Materials Research* 45 (2), 108-116.
- Ziv, V., Weiner, S., 1994. Bone crystal sizes: a comparison of transmission electron microscopic and X-ray diffraction line width broadening techniques. *Connective Tissue Research* 30 (3), 165-175.